

Propagation Failure Along Myelinated Nerves

A. Carpio & I. Peral

Journal of Nonlinear Science

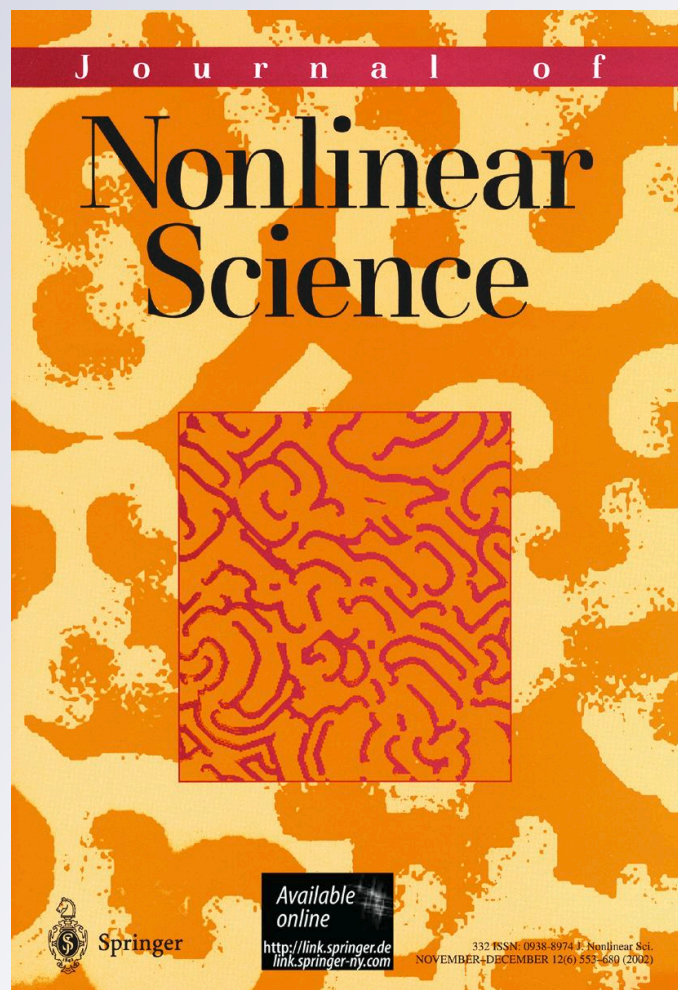
ISSN 0938-8974

Volume 21

Number 4

J Nonlinear Sci (2011) 21:499-520

DOI 10.1007/s00332-010-9090-x



Your article is protected by copyright and all rights are held exclusively by Springer Science+Business Media, LLC. This e-offprint is for personal use only and shall not be self-archived in electronic repositories. If you wish to self-archive your work, please use the accepted author's version for posting to your own website or your institution's repository. You may further deposit the accepted author's version on a funder's repository at a funder's request, provided it is not made publicly available until 12 months after publication.

Propagation Failure Along Myelinated Nerves

A. Carpio · I. Peral

Received: 6 December 2009 / Accepted: 22 December 2010 / Published online: 7 February 2011
© Springer Science+Business Media, LLC 2011

Abstract Propagation of traveling pulses in the myelinated Hodgkin–Huxley model is studied. The nerve impulse is a traveling wave with two components. At the Ranvier nodes, it behaves as a discrete traveling pulse. Wave motion through the internodal regions is then driven by this traveling pulse. We give analytical characterizations of the parameter ranges for which nerve impulses fail to propagate by exploiting time scale separation and the active node approximation, which reduces the dynamics of infinite fibers to the evolution of a few nodes. Simple recipes to predict the speed of the impulses and the widths of their peaks are also given. Predictions are in good agreement with the information provided by numerical simulations.

Keywords Travelling waves · Propagation failure · Myelinated nerves · Reaction–diffusion systems

Mathematics Subject Classification (2000) 92B05 · 35K57 · 34K31 · 34K60

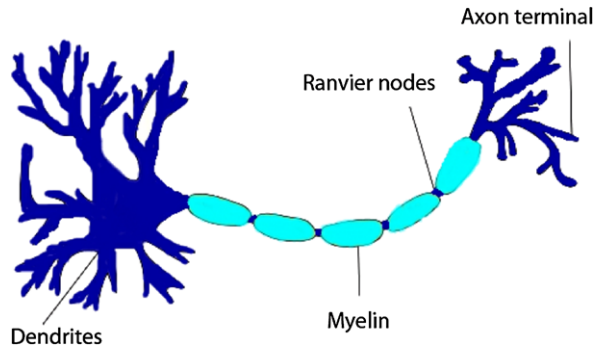
1 Introduction

Understanding the role of the relevant control variables in nerve impulse propagation may help to devise strategies to improve the life quality of people suffering from multiple sclerosis or other nerve diseases (Pluchino et al. 2003). Often, nerve propagation

Communicated by P.K. Maini.

A. Carpio (✉) · I. Peral
Departamento de Matemática Aplicada, Universidad Complutense de Madrid, Madrid 28040, Spain
e-mail: ana_carpio@mat.ucm.es

Fig. 1 Structure of a myelinated neuron



failure is due to damage in the myelin sheaths covering the axons of motor neurons (Moore et al. 1978; Rushton 1951; Struijk 1997; Scott 2002). Each neuron is formed by a cell body and an axon; see Fig. 1. Unlike nerve fibers in primitive animals (such as squids), the neurons of vertebrates are myelinated. This means that the axon is almost entirely covered by insulating layers of myelin. The sheath of myelin is periodically interrupted by Ranvier nodes, at which the nerve membrane is exposed and the interchange of ions with the surrounding medium can take place. External stimuli generate a nerve impulse. When this impulse surpasses a threshold, it jumps from node to node, giving rise to ‘saltatory’ wave propagation along the axon (FitzHugh 1962; Keener 2000; Scott 2002). The alternance of myelin sheaths and nodes allows for high conduction speeds in fibers of small diameter. In unmyelinated nerves, fast propagation of impulses is only possible by increasing the diameter (Goldman and Albus 1968; Scott 1975). Nerve propagation along myelinated fibers can be modeled by a system of ordinary differential equations for the Ranvier nodes coupled with a diffusion equation at the internodes (FitzHugh 1962; Markin and Chimadzhiev 1967; Pickard 1966), the ‘myelinated Hodgkin–Huxley’ (MHH) model. Careful computational studies have shown a reasonable agreement of the numerically observed propagation speeds with experimental measurements for toads or frogs (FitzHugh 1962; Goldman and Albus 1968; Moore et al. 1978). Related approaches to saltatory propagation have been tried in the study of calcium waves and cardiac muscles. The fire-diffuse-fire models employed in this field consist of diffusion equations loaded with point sources (Coombes et al. 2003; Ponce et al. 1999). Recently, such models have been applied to the study of synaptic transmission between neurons (Timofeeva 2010).

Analytical work on nerve conduction has mostly focused on models for unmyelinated axons: the Hodgkin–Huxley (HH) model (Casten et al. 1975; Hodgkin and Huxley 1952; Muratov 2000) and simplified FitzHugh–Nagumo (FHN) or Nagumo equations (FitzHugh 1961; Nagumo et al. 1962; Rinzel and Keller 1973; Scott 1975). Nerve impulses are described mathematically by traveling wave solutions of the partial differential equations defining such models. Explicit constructions (Rinzel and Keller 1973) and asymptotic studies (Casten et al. 1975; Keener 1980; Muratov 2000) provide predictions of their speeds in terms of the parameters. The voltage is a fast excitable variable: it jumps abruptly from the resting state to an excited value and then returns to equilibrium. Some of the variables governing the ki-

netics of the ion currents evolve on a slower time scale, allowing for recovery. Propagation failure in unmyelinated nerves occurs only when the separation of time scales between the fast excitable variables and the slow recovery variables is too small.

Propagation criteria for myelinated versions of the Nagumo and FitzHugh–Nagumo equations (with partial differentials replaced by finite differences) are established in Anderson and Sleeman (1995), Bell and Costner (1984), Keener (2000). Discrete models with a similar mathematical structure but Morris–Lecar or Beeler–Reuter dynamics might help to understand excitable behavior in muscles and cardiac tissue (Beeler and Reuter 1977; Carpio 2005b; Keener 2000; Keener and Sneyd 1998; Morris and Lecar 1981). Asymptotic and explicit constructions of impulses are presented in Carpio and Bonilla (2001, 2003b), Carpio (2005a), Fáth (1998), Tonnelier (2003). Models coupling two myelinated nerves, which can serve as a basis to study nerve bundles are discussed in Binczak et al. (2001). All these simplified models are easier to analyze, but have the disadvantage of being inaccurate. More realistic models, such as the MHH equations, provide quantitative information but have a complicated structure. Up to now, the understanding of realistic models was mainly based on time-consuming numerical simulations. In this paper, we propose a ‘semi-analytical’ technique to extract quantitative predictions out of the MHH model without performing costly numerical tests. An approximation of saltatory impulses based on time scale separation and the idea of an ‘active node’ (Carpio and Bonilla 2003b) yields quantitative predictions of the propagation speed and the range of parameters for which propagation fails. This happens due to inadequate time scale separation for the kinetics of the voltage and ion currents, but also to alterations in the myelin sheath.

The paper is organized as follows. In Sect. 2 we formulate the MHH model in two equivalent forms: the original diffusion equation periodically coupled with the dynamics of the Ranvier nodes, and a closed integrodifferential system of equations for the nodes which is useful to understand the structure of wave solutions. We work with realistic parameter values for frogs and toads, for which spatial discreteness is relevant. Section 3 contains a numerical description of impulses, identified with wave solutions of a peculiar structure. At the Ranvier nodes, they are described by a discrete traveling pulse solution of the integrodifferential system. The evolution of the action potential in the internodal region is driven by the dynamics of the nodes. The leading front of the pulse solves a reduced bistable system involving two fast variables, instead of a bistable equation for the voltage as in simplified FitzHugh–Nagumo or Nagumo models. Predictions of parameter ranges for propagation failure are given in Sects. 4 and 5, exploiting separation of time scales and the analysis of truncated systems involving a few nodes. Whereas Sect. 4 focuses on pinning of the leading front of the impulses, Sect. 5 deals with failure due to inadequate time scale separation. Unlike previous work on propagation failure (Anderson and Sleeman 1995; Keener 2000) in spatially discrete systems, which relies on comparison principles for bistable equations or holds near averaged limits excluding saltatory propagation, our strategy is successful in systems for which no principles for comparison are known and discreteness is relevant. Moreover, our predictions are sharp. Section 6 summarizes our conclusions. Final Appendices A, B, C contain additional material on the nondimensionalization of the model, the structure of the integrodifferential equations for the nodes and the procedure employed to construct numerical solutions.

Table 1 Dimensionless parameters for a myelinated frog nerve

D_c	D_d	R	g_{Na}	g_K	g_L	V_K	V_L	λ_h	λ_n
0.082	0.175	58.92	2.99	0.546	0.131	-0.043	-0.043	0.014	0.016

2 The Myelinated Hodgkin–Huxley Model

The dimensionless MHH model couples a diffusion equation for the dimensionless voltage in the internodal regions,

$$\frac{\partial v}{\partial t} = D_c \frac{\partial^2 v}{\partial x^2} - \frac{v}{R}, \quad x \in (x_j, x_{j+1}) = (j, j + 1), \quad t > 0, \tag{1}$$

$$v(x_j, t) = v_j(t), \quad v(x_{j+1}, t) = v_{j+1}(t), \tag{2}$$

with a sequence of ordinary differential equations describing the dynamics of the nodes (located at integer positions $x_j = j$):

$$\begin{aligned} \frac{dv_j}{dt} + g_{Na} m_j^3 h_j (v_j - 1) + g_L (v_j - V_L) + g_K n_j^4 (v_j - V_K) \\ = D_d \left[\frac{\partial v}{\partial x} (x_j^+, t) - \frac{\partial v}{\partial x} (x_j^-, t) \right], \end{aligned} \tag{3}$$

$$\frac{dm_j}{dt} = \Lambda_m(v_j) [m_\infty(v_j) - m_j],$$

$$\frac{dn_j}{dt} = \lambda_n \Lambda_n(v_j) [n_\infty(v_j) - n_j], \tag{4}$$

$$\frac{dh_j}{dt} = \lambda_h \Lambda_h(v_j) [h_\infty(v_j) - h_j],$$

where v_j represents the dimensionless voltage at the j th node and m_j, n_j, h_j control the sodium and potassium activation and the sodium inactivation, respectively. The dimensionless ion current acts as a source:

$$I_{ion}(v_j, m_j, n_j, h_j) = g_{Na} m_j^3 h_j (v_j - 1) + g_L (v_j - V_L) + g_K n_j^4 (v_j - V_K).$$

Table 1 collects parameter values for frogs representing dimensionless diffusivities D_c, D_d , resistances R , conductances g_{Na}, g_K, g_L (Na stands for sodium, K for potassium, L for leakage) and voltages V_K, V_L . The procedure followed to nondimensionalize the model together with explicit expressions for the rate functions $\Lambda_n(v), \Lambda_m(v), \Lambda_h(v)$ and the equilibrium states $n_\infty(v), m_\infty(v), h_\infty(v)$ are given in Appendix A. λ_h, λ_n control time scale separation, since the profiles $\Lambda_h, \Lambda_n, \Lambda_m$ are of order one in the ranges of interest.

The structure of the wave solutions of the MHH model is better understood by reformulating the original model as a closed system of differential equations for the Ranvier nodes. Time dependent solutions of (1)–(2) can be expressed as Fourier series of the initial $v(x, 0)$ and boundary values $v_j(t), v_{j+1}(t)$, which represent

the voltage at the Ranvier nodes. For each fixed $v_j(t), v_{j+1}(t)$, we denote by $v = Q[v_j, v_{j+1}](x, t)$ the solution of (1)–(2). We set $G^+(v_j, v_{j+1}) = \frac{\partial Q[v_j, v_{j+1}]}{\partial x}(x_j^+, t)$ and $G^-(v_{j-1}, v_j) = \frac{\partial Q[v_{j-1}, v_j]}{\partial x}(x_j^-, t)$. Then, (3) can be rewritten as

$$\frac{dv_j}{dt} + I_{ion}(v_j, m_j, n_j, h_j) = D_d[G^+(v_j, v_{j+1}) - G^-(v_{j-1}, v_j)]. \tag{5}$$

Equations (4) and (5) form an integrodifferential system for v_j, m_j, h_j , and n_j at the Ranvier nodes. Integral expressions for the operator $G^+(v_j, v_{j+1}) - G^-(v_{j-1}, v_j)$ are given in Appendix B for the sake of completeness. We will not make use of those explicit formulas for the time dependent case. When time dependence can be neglected, the structure of this operator simplifies. These simpler expressions will be relevant in the sequel and we detail them below.

In case we look for equilibrium states, the time derivative v_t in (1) vanishes. The corresponding stationary solution $Q[v_j, v_{j+1}]$ of (1)–(2) is

$$Q[v_j, v_{j+1}](x) = Ae^{\gamma(x-x_j)} + Be^{-\gamma(x-x_j)},$$

$$A = \frac{v_j e^{-\gamma} - v_{j+1}}{e^{-\gamma} - e^{\gamma}}, \quad B = \frac{v_{j+1} - v_j e^{\gamma}}{e^{-\gamma} - e^{\gamma}}, \quad \gamma = \frac{1}{\sqrt{D_c R}}. \tag{6}$$

In this way, the internodal voltage is expressed as a function of the constant voltage at the Ranvier nodes. We may now compute

$$G^+(v_j, v_{j+1}) - G^-(v_{j-1}, v_j) = \frac{\partial Q[v_j, v_{j+1}]}{\partial x}(x_j^+, t) - \frac{\partial Q[v_{j-1}, v_j]}{\partial x}(x_j^-, t)$$

$$= (v_{j+1} - v_j(e^{\gamma} + e^{-\gamma}) + v_{j-1}) \frac{2\gamma}{e^{\gamma} - e^{-\gamma}}.$$

Since $\frac{dv_j}{dt} = 0$, (5) becomes a nonlinear system for the stationary states:

$$g_{Na} m_j^3 h_j (v_j - 1) + g_L (v_j - V_L) + g_K n_j^4 (v_j - V_K)$$

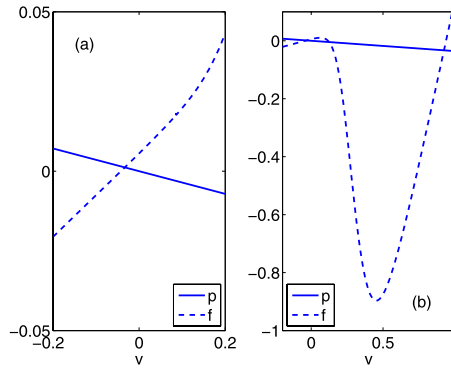
$$= \frac{2D_d \gamma}{e^{\gamma} - e^{-\gamma}} (v_{j+1} - 2v_j(e^{\gamma} + e^{-\gamma}) + v_{j-1}). \tag{7}$$

If the nerve is initially at equilibrium and $v_j(t), v_{j+1}(t)$ are known to vary very slowly with time, we may neglect again v_t in (1)–(2). In this quasistatic approximation, the internodal voltage is again given by (6), with v_j, v_{j+1} replaced by $v_j(t), v_{j+1}(t)$.

3 Construction of Nerve Impulses

The MHH system (1)–(4), or equivalently (4)–(5), describes propagation of impulses when it has an excitable nature. This means that there is a stable equilibrium, and that sufficiently large disturbances from this equilibrium give rise to large excursions of the variables before they return to equilibrium.

Fig. 2 (a) Calculation of the resting state of the nerve. (b) Calculation of the maximum value for the action potential



System (1)–(4) has a unique equilibrium state $v_j = v^*$, $n_j = n^*$, $m_j = m^*$, $h_j = h^*$ when v^* , $n^* = n_\infty(v^*)$, $m^* = m_\infty(v^*)$ and $h^* = h_\infty(v^*)$ solve (7), which yields an equation for v^* :

$$f(v^*) = p(v^*),$$

$$p(s) = 2D_d\gamma \frac{1 - \cosh(\gamma)}{\sinh(\gamma)}s, \quad \gamma = \frac{1}{\sqrt{D_c R}}, \tag{8}$$

$$f(s) = g_{Na}(m_\infty(s))^3 h_\infty(s)(s - 1) + g_L(s - V_L) + g_K(n_\infty(s))^4 (s - V_K).$$

Figure 2(a) plots $f(s)$ and $p(s)$ for the parameter values in Table 1. The graph of $p(s)$ cuts $f(s)$ at $(v^*, f(v^*))$, with $v^* < 0$.

Once we have determined v^* , the internodal voltage is given by

$$v^* \frac{e^{-\gamma} - 1}{e^{-\gamma} - e^\gamma} e^{\gamma(x-x_j)} + v^* \frac{1 - e^\gamma}{e^{-\gamma} - e^\gamma} e^{-\gamma(x-x_j)}, \quad \gamma = \frac{1}{\sqrt{D_c R}}.$$

This equilibrium state is linearly stable for the dynamics (1)–(4). This can be checked by linearizing about it and then looking for solutions of the linearized problem with the structure $(v_j, n_j, m_j, h_j)e^{\alpha t}$, $v(x)e^{\alpha t}$. Inserting these expressions in the linearized equations, we find an eigenvalue problem for α and the prefactors (v_j, n_j, m_j, h_j) , $v(x)$. A numerical study of this eigenvalue problem suggests that $\text{Re } \alpha < 0$ and the equilibrium state is linearly stable.

Figures 3–7 illustrate the structure of the impulse generated exciting the node $j = 0$ for a short time, in a nerve initially at rest. These figures have been generated solving the dimensionless MHH equations by the method of lines; see Appendix C for details. We discretize by finite differences the derivatives appearing in (1) and (3), and solve the resulting system of ordinary differential equations for the voltage at the numerical nodes, coupled with the system for the voltage at the Ranvier nodes.

Figures 3 and 5 show the structure of the nerve impulse propagating along the fiber. Notice that a single Ranvier node is crossing the gap from the resting voltage to the excited voltage at each stage. Once this node has reached the excited voltage, the next node moves away from the resting state. The resulting wave front motion is ‘saltatory’. Figures 4 and 6 plot the temporal profile of the impulse. Adjacent

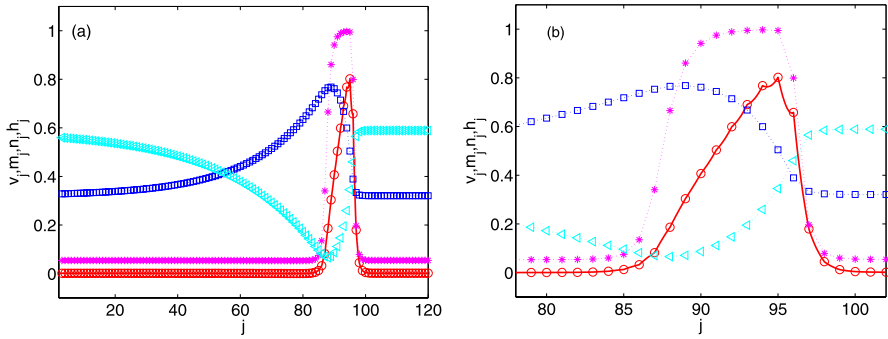


Fig. 3 (a) Spatial profile of the nerve impulse at the Ranvier nodes for a fixed time: v_j (circles), m_j (asterisks), h_j (triangles), n_j (squares). The solid line represents the evolution of the potential in internodal regions. (b) Zoom in the peak region. Parameter values are given in Table 1

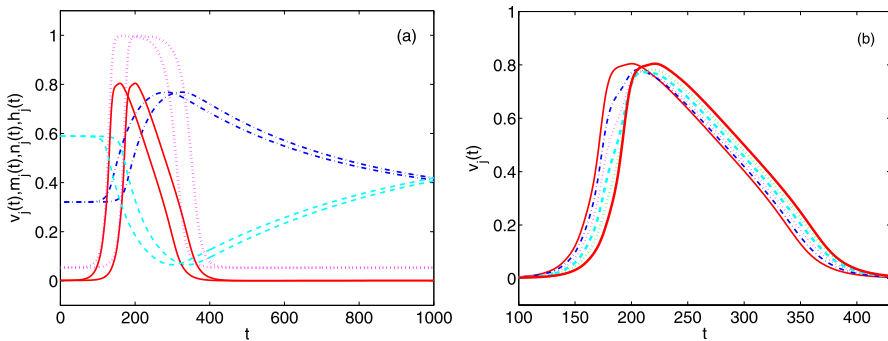
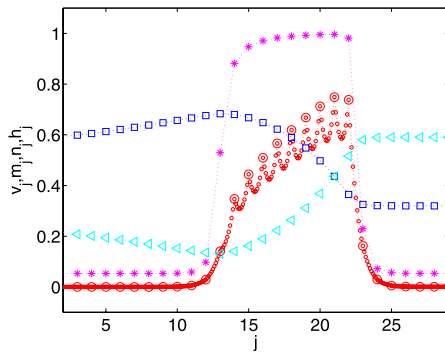


Fig. 4 (a) Temporal profile of the nerve impulse at two fixed consecutive Ranvier nodes: v_j (solid line), m_j (dotted), h_j (dashed), n_j (dash-dotted). (b) Zoom at the voltage peak, including the voltage at four intermediate numerical nodes located in the myelin sheath (dashed lines). Parameter values given in Table 1

Fig. 5 Spatial profile of the nerve impulse at the Ranvier nodes for a fixed time: v_j (large circles), m_j (asterisks), h_j (triangles), n_j (squares). Small circles represent the evolution of the voltage in the myelin sheaths (at the numerical nodes). Parameter values are given in Table 1 with R replaced by $R/10$, and λ_n, λ_h by $\lambda_n/4, \lambda_h/4$



nodes undergo the same evolution with a constant delay. At the numerical nodes introduced between two adjacent Ranvier nodes the temporal profile varies slightly; see Figs. 4(b) and 6(b). Such small variations influence the tails and fronts of the spatial

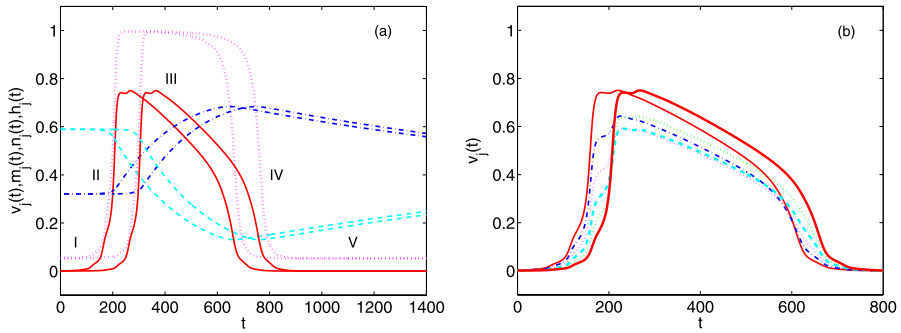


Fig. 6 (a) Temporal profile of the nerve impulse at two consecutive Ranvier nodes: v_j (solid line), m_j (dotted), h_j (dashed), n_j (dash-dotted). (b) Zoom at the voltage peak, including the voltage at four intermediate numerical nodes located in the myelin sheath (dashed lines). Parameter values are given in Table 1 with R replaced by $R/10$, and λ_n, λ_h by $\lambda_n/4, \lambda_h/4$

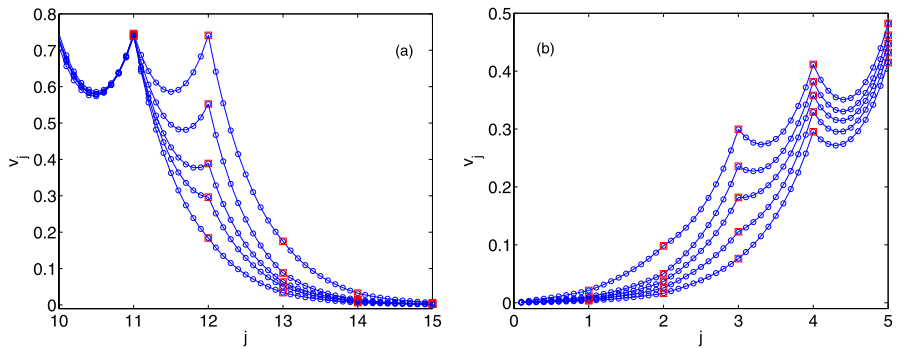


Fig. 7 (a) Propagation of the front of the voltage pulse along the axon as time grows. (b) Evolution of the tail. Squares correspond to Ranvier nodes and circles to numerical nodes within the myelin sheath

profiles; see Fig. 7. Temporal profiles are the same for numerical nodes occupying the same position in different internodes. These numerical simulations suggest that impulses behave like some kind of traveling wave.

When space is continuous, traveling waves are given by $u(x, t) = u(x - ct)$. All the points x undergo the same evolution as time grows with a time delay τ . Plotting $u(x - ct)$ for different fixed times and $c > 0$, we see a pattern moving to the right at speed c . In a spatially discrete system, a traveling wave has the mathematical structure $u_j(t) = u(j - ct)$. All nodes j evolve according to the same profile, with a delay $\tau = \frac{1}{c}$ between consecutive nodes: $u_{j+1}(t) = u(j + 1 - ct) = u(j - c(t - 1/c)) = u_j(t - \frac{1}{c})$.

The original MHH model has a hybrid structure, mixing spatially discrete and continuous variables. Using the integrodifferential system for the Ranvier nodes (4)–(5), the continuous and discrete components uncouple. The structure of the traveling pulses becomes clear. At the Ranvier nodes, the variables evolve as discrete wave solutions of system (4)–(5): $v_j(t) = v(j - ct)$, $m_j(t) = m(j - ct)$,

$n_j(t) = n(j - ct)$, $h_j(t) = h(j - ct)$. The evolution of the internodal region is driven by the nodes: $v(x, t) = w(x - [x], t - [x]/c)$ ($[]$ denotes the integer part, that is: $x = [x] + r$, $0 \leq r < 1$), where the profile $w(z, t)$ solves

$$\frac{\partial w}{\partial t} = D_c \frac{\partial^2 w}{\partial z^2} - \frac{w}{R}, \quad z \in (0, 1), \quad t > 0, \tag{9}$$

$$w(0, t) = v(-ct), \quad w(1, t) = v(1 - ct). \tag{10}$$

All the points x, y located in internodal regions and placed at the same distance of their respective left nodes undergo the same evolution with a time delay $(x - y)/c$. Therefore, describing a nerve impulse reduces to analyzing traveling pulse solutions of (4)–(5).

4 Propagation Failure Due to Pinning of the Leading Front

Quantitative predictions of the propagation speed and the ranges of parameters for which propagation fails are obtained exploiting two facts.

- The presence of two separate time scales (Carpio 2005a; Casten et al. 1975; Muratov 2000). The fast variables v_j and m_j evolve in the fast time scale t . The slow variables n_j and h_j vary in a slower time scale $\tau = \epsilon t$, $\epsilon = \lambda_n \sim 10^{-2}$ (see Table 1, we set $\lambda_h = \lambda_\epsilon$).
- The small size of $D_d \sim 10^{-1}$ (see Table 1). This results in ‘saltatory’ propagation (node by node) and renders useless approximations of (3) or (5) in which their right hand sides are crudely replaced by $D_d \frac{\partial^2 v}{\partial x^2}$.

Figure 6(a) depicts different regions in the time profile of the nerve impulse. Initially, the nerve is at rest (I), in the equilibrium state (v^*, m^*, n^*, h^*) . The onset of the impulse is a front, marked as (II). The next region is the peak of the pulse, marked (III). The fourth and the fifth regions describe the return to the resting state. This section is devoted to the analysis of propagation failure due to pinning of the leading front. By ‘pinning’, we mean that the leading front is trapped at a node and cannot move, so that stable pulses cannot be formed.

In the leading front (region (II)), the slow variables remain approximately at their rest values (n^*, h^*) . The smaller ϵ is, the more accurate this approximation becomes. The fast variables jump abruptly from their rest values (v^*, m^*) to an excited state (V, M) , forming a front for the fast system:

$$\frac{dv_j}{dt} + I_{ion}(v_j, m_j, n^*, h^*) = D_d [G^+(v_j, v_{j+1}) - G^-(v_{j-1}, v_j)], \tag{11}$$

$$\frac{dm_j}{dt} = \Lambda_m(v_j) [m_\infty(v_j) - m_j]. \tag{12}$$

The system (11)–(12) has three equilibrium states. The leading front joins the two stable equilibria: (v^*, m^*) and (V, M) , $M = m_\infty(V)$, where V solves

$$f(V) = p(V),$$

$$p(s) = 2D_d\gamma \frac{1 - \cosh(\gamma)}{\sinh(\gamma)} s, \quad \gamma = \frac{1}{\sqrt{D_c R}}, \tag{13}$$

$$f(s) = g_{Na}(m_\infty(s))^3 h^*(s - 1) + g_L(s - V_L) + g_K(n^*)^4 (s - V_K).$$

The graphs of f and p are depicted in Fig. 2(b), showing three possible solutions. The first one is $v^{(1)} = v^*$ and the third one $v^{(3)} = V$. The intermediate value $v^{(2)}$ marks a threshold for stability. The intensity of the excitation at the left node $j = 0$ must surpass $v^{(2)}$ for an impulse to be generated. Wave front solutions of (11)–(12) may either be stationary or they may propagate. Only in the second case can the nerve impulse propagate successfully.

To determine ranges of parameters for which the leading front propagates we use the ‘active point’ approximation (Carpio and Bonilla 2001, 2003a, 2003b). This method was developed for wave fronts in discrete bistable equations and is recalled in Sect. 4.1. Section 4.2 applies a similar strategy to our fast system.

4.1 Active Point Theory for Bistable Equations

Let us consider a spatially discrete bistable equation:

$$\frac{dv_j}{dt} = D(v_{j+1} - 2v_j + v_{j-1}) - f(v_j) - w, \quad D > 0, \quad j \in \mathbb{Z}. \tag{14}$$

The sources $f(z) + w$ have three zeros $z_1(w) < z_2(w) < z_3(w)$ (the first and the third of which are stable) provided $w \in (w_{\min}, w_{\max})$. w is a parameter controlling the symmetry of the source. Analytical and numerical studies of wave front solutions joining z_1 and z_3 (see Carpio et al. 2000; Carpio and Bonilla 2001, 2003a; F ath 1998; Mallet-Paret 1999; Zinner 1992 and references therein) suggest that, generically, there are two threshold values $w_{c-}(D)$, $w_{c+}(D)$ such that we have the following.

- If $w \in (w_{\min}, w_{c-}(D))$, there exist wave front solutions $v_j(t) = v(j - ct)$ decreasing from $z_3(w)$ to $z_1(w)$ (resp. increasing from $z_1(w)$ to $z_3(w)$) moving to the right (resp. left) with speed $c = c_+(w, D) \neq 0$.
- If $w \in (w_{c+}(D), w_{\max})$, there exist wave front solutions increasing from $z_1(w)$ to $z_3(w)$ (resp. decreasing from $z_3(w)$ to $z_1(w)$) moving to the right (resp. left) with speed $c = c_-(w, D) \neq 0$.
- If $w \in [w_{c-}(D), w_{c+}(D)]$, there exist static wave front solutions ($c = 0$). The size of this interval grows as D decreases, hindering propagation.

For sources $-\sin(z) - w$, it was proven that static and moving wave fronts cannot coexist for the same values of D and w (Carpio et al. 2000). Similar arguments seem to apply to more general sources $f(z, w)$. Moreover, comparison principles using static or moving wave fronts as sub- or supersolutions to block or force propagation seem to imply that wave front propagation is not possible when static wave fronts exist.

For exceptional sources, it may happen that $w_{c-}(D) = w_{c+}(D)$, but then saltatory propagation is excluded (Carpio and Bonilla 2003a).

At $w_{c\pm}(D)$ the so-called depinning transitions occur. For small D , there are stable static fronts s_j at $w = w_{c-}(D)$ with the following structure: two essentially constant tails $s_j \sim z_3(w)$, $j < 0$, and $s_j \sim z_1(w)$, $j > 0$, joined by an *active* point s_0 , which takes values in the interval $(z_1(w), z_2(w))$. As we vary w , such static ('pinned') fronts cease to exist and propagation becomes possible. While the wave front patterns move at a constant speed c for $w < w_{c-}(D)$, the motion of individual points $v_j(t)$ belonging to moving fronts is saltatory. Their spatial profiles v_j stay near some shifted static configuration $s_{j-\ell}$, for a time of order $\frac{1}{c}$, until the ℓ th point $v_\ell(t)$ (the *active point*) jumps from s_0 to $z_3(w)$ and $v_{\ell+1}(t)$ (the *next active point*) jumps from $z_1(w)$ to s_0 , advancing the front one position (Carpio and Bonilla 2003a; Fáth 1998).

The depinning transition occurs when the branches of static wave fronts undergo a bifurcation of saddle-node type. This fact can be sustained by truncation to finite dimension (Carpio and Bonilla 2003a). If D is small, the sequence of equations is truncated to one for the active point:

$$\frac{dv_0}{dt} = D(z_1(w) - 2v_0 + z_3(w)) - f(v_0) - w. \tag{15}$$

This equation has three stationary solutions if $w_-(D) < w < w_+(D)$, two stable and one unstable. Setting s_0 equal to any of those stationary solutions, $s_j = z_3(w)$, $j < 0$, and $s_j = z_1(w)$, $j > 0$, we reconstruct the static wave fronts of (14). At $w = w_-(D)$, the two solutions close to $z_1(w)$ collide. For $w < w_-(D)$, only the stable solution near $z_3(w)$ is left. An analogous situation is encountered for $w > w_+(D)$. The values $w_\pm(D)$ approximate the thresholds $w_{c\pm}(D)$ of (14). The speed and profiles of the traveling wave solutions of (14) near $w = w_\pm(D)$ are predicted by using the normal form of the bifurcation and matched asymptotic expansions (Carpio and Bonilla 2003a). Near the thresholds, the temporal wave profiles are staircase like, and the speed is approximated by the inverse of the time spent in one step, which is predicted using the blow-up time of the normal form.

An analogous situation is encountered as D increases, with a larger number of active points filling the gap between the constant tails, see Carpio and Bonilla (2003a), Fáth (1998).

An identical analysis is hard to reproduce in our case, due to the coupling with the diffusion equation. However, we can exploit the underlying strategy to predict propagation thresholds and speeds.

4.2 Analysis of the Leading Front

For small ε , the leading front of the impulse has the structure (v_j, m_j, n^*, h^*) , where (v_j, m_j) is a front for the fast system (11)–(12). Notice that the diffusivity $D_d = (C_n \bar{\lambda}_M (\bar{R}_e + \bar{R}_i) L)^{-1} \sim 10^{-1}$ takes small values. Due to this fact, most of the time such fronts consist essentially of two constant tails joined by one node, at which the voltage jumps from the rest state v^* to an excited state V . This suggests that an

approximation using one or two active points might be tried. Figures 3, 5 and 7 seem to validate this assumption.

To determine the threshold parameters for failure, truncation to a system involving just one node is enough. If the active point is located at $j = j_0$, the reduced equations are

$$\frac{dv_{j_0}}{dt} + I_{ion}(v_{j_0}, m_{j_0}, n^*, h^*) = D_d[G^+(v_{j_0}, v^*) - G^-(V, v_{j_0})], \tag{16}$$

$$\frac{dm_{j_0}}{dt} = \Lambda_m(v_{j_0})[m_\infty(v_{j_0}) - m_{j_0}]. \tag{17}$$

In case static wave front solutions of the full fast system exist, they may be approximated by two constant states joined by the active node:

$$\begin{aligned} m_j &= M, & j < j_0, & & m_{j_0}, & & m_j = m^*, & j > j_0, \\ v_j &= V, & j < j_0, & & v_{j_0}, & & v_j = v^*, & j > j_0. \end{aligned} \tag{18}$$

The unknown values (v_{j_0}, m_{j_0}) are stationary solutions of (16)–(17), satisfying $m_\infty(v_{j_0}) = m_{j_0}$ and

$$I_{ion}(v_{j_0}, m_\infty(v_{j_0}), n^*, h^*) = D_d[G^+(v_{j_0}, v^*) - G^-(V, v_{j_0})]. \tag{19}$$

For time independent arguments, the operators G^+ and G^- are explicitly defined at the end of Sect. 2. Equation (19) becomes

$$\begin{aligned} &g_{Na}m_\infty(v_{j_0})^3h^*(v_{j_0} - 1) + g_L(v_{j_0} - V_L) + g_K(n^*)^4(v_{j_0} - V_K) \\ &= \frac{2D_d\gamma}{e^\gamma - e^{-\gamma}}(V - v_{j_0}(e^\gamma + e^{-\gamma}) + v^*), \quad \gamma = \frac{1}{\sqrt{D_cR}}. \end{aligned} \tag{20}$$

Notice that (v^*, n^*, h^*, V) are not fixed but depend on the parameters. For typical parameter values, (20) has either one or three solutions. When it has three solutions, the solution v closest to v^* can be used to approximate the static wave front solution of (11)–(12) generated by exciting the left end of a chain of nodes: an initial state at equilibrium evolves into a static wave front with a left tail near (V, M) and a right tail near (v^*, m^*) , joined by $(v, m_\infty(v))$.

Unlike the situation described in Sect. 4.1, for the fast system (11)–(12) we lack rigorous results relating propagation success or failure to the existence of stationary or traveling waves, or establishing that static and moving waves cannot coexist. Assuming that this is still the situation, we use identity (20) to predict ranges of parameters for which propagation fails, as in Sect. 4.1. As long as (20) has three solutions, propagation of wave fronts in (11)–(12) should be blocked and nerve impulses would fail to propagate. Figure 8(a) plots the resulting threshold value of R for propagation failure as a function of g_{Na} . At such thresholds, the two solutions of (20) which are close to v^* are lost. There is good agreement between this curve and the one obtained by directly checking whether an impulse is generated by exciting the left end of a chain of nodes governed by the full system (1)–(4) during a long enough time (up to 10–50 in our tests) for small enough ε . Notice that we only expect this approximation

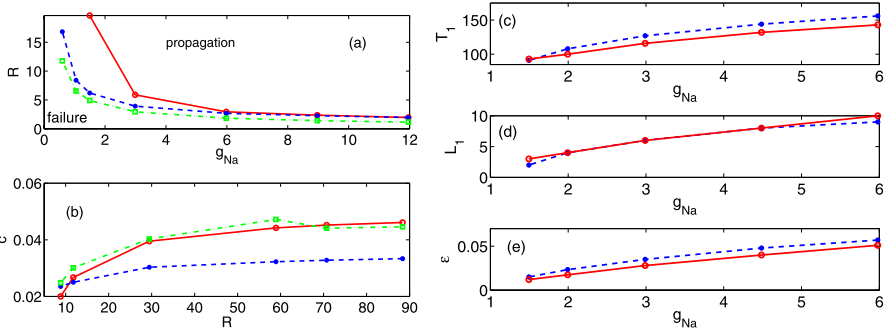


Fig. 8 (a) Threshold curve for propagation (*dashed*) obtained studying the solutions of (20), compared to the curve computed by direct simulation of impulses using (1)–(4) with parameters given in Table 1 (*solid*) or smaller $\lambda_n/10$, $\lambda_h/10$ (*dash-dotted*). (b) Numerically calculated speeds of the impulses. The *solid* curve is computed solving the full system (1)–(4). The *dashed* and *dashed-dotted* lines are predictions obtained by numerically solving the active node approximations with one node (16)–(17) and two nodes (21)–(24), respectively. (c) Peak time length, (d) number of nodes in a peak and (e) threshold separation of time scales for propagation of stable impulses calculated by direct simulation (*solid lines*) of (1)–(4) compared to the predictions (*dashed lines*) given by (31), (32) and (33), respectively. Reference parameters for (b), (c), (d), (e) are given in Table 1. All the magnitudes are dimensionless. Dimensions can be restored as described in Appendix A

to perform well when λ_n and λ_h are small enough to ensure an adequate time scale separation and D_d is small enough to justify truncation to one active point. The quality of the approximation as D_d grows can be improved by considering two or more active points and studying when the truncated problems loose blocking static wave fronts. For λ_n and λ_h given in Table 1, the approximation worsens as g_{Na} decreases because the mechanisms for propagation failure described in Sect. 5 become relevant (vanishing peak length due to insufficient time scale separation instead of pinning of leading front). Similar plots may be obtained for other sets of parameters.

When (20) loses its two smallest solutions, the dynamic equations for the active point (16)–(17) drive an initial state (v^*, m^*) to a state close to (V, M) . The resulting trajectories $(v_{j_0}(t), m_{j_0}(t))$ approximate quite well the trajectories $(v_j(t), m_j(t))$ generated by exciting (1)–(4) in Sect. 3 (up to a time shift). We obtain a rough prediction of the speed of the front by computing the inverse of the time an active point takes to first reach (V, M) . This arrival time is calculated by numerically solving (16)–(17), choosing as initial data (v^*, m^*) at time zero. This value is finite, because the trajectories are not monotonic: the values V and M are surpassed and then the profiles decrease to their limit. The prediction improves as we approach the thresholds for failure, since it is reminiscent of the estimation of the time spent in steps of the profile mentioned in Sect. 4.1 (Carpio and Bonilla 2003a). For standard values of the parameters, a sharper approximation is found by truncating the fast system (11)–(12) to two active points located at $j = j_0, j_0 + 1$, with $v_{j_0-1} = V, v_{j_0+2} = v^*$:

$$\frac{dv_{j_0}}{dt} + I_{ion}(v_{j_0}, m_{j_0}, n^*, h^*) = D_d[G^+(v_{j_0}, v_{j_0+1}) - G^-(V, v_{j_0})], \tag{21}$$

$$\frac{dv_{j_0+1}}{dt} + I_{ion}(v_{j_0+1}, m_{j_0+1}, n^*, h^*) = D_d[G^+(v_{j_0+1}, v^*) - G^-(v_{j_0}, v_{j_0+1})], \tag{22}$$

$$\frac{dm_{j_0}}{dt} = \Lambda_m(v_{j_0})[m_\infty(v_{j_0}) - m_{j_0}], \tag{23}$$

$$\frac{dm_{j_0+1}}{dt} = \Lambda_m(v_{j_0+1})[m_\infty(v_{j_0+1}) - m_{j_0+1}]. \tag{24}$$

Starting from (v^*, v^*, m^*, m^*) at time zero, the corresponding numerical solutions reach values near (V, V, M, M) as time grows. The trajectories $v_{j_0}(t)$, $v_{j_0+1}(t)$ look alike, except for a time lag. Let t_1 and t_2 be the times at which both reach the same value $v_{j_0}(t_1) = v_{j_0+1}(t_2) = \frac{v^*+V}{2}$. Then, the speed of the wave fronts governed by (11)–(12) can be approximated by $c \sim \frac{1}{t_2-t_1}$ (provided D is small enough), and so can the speed of the impulses generated by the whole system (provided ε is small enough). Figure 8(b) shows good agreement between this second prediction and the speed of pulses for the parameter values in Table 1.

4.3 Comparison with Simpler Models

Simplified versions of the MHH model assume the axial current to be constant along the myelin sheath: $\frac{\partial v}{\partial x}(x, t) = v_{j+1}(t) - v_j(t)$ in $[j, j + 1]$. We obtain the discrete Hodgkin–Huxley (DHH) model at the nodes, given by (4) and:

$$\frac{dv_j}{dt} + I_{ion}(v_j, m_j, n_j, h_j) = D_d(v_{j+1} - 2v_j + v_{j-1}). \tag{25}$$

The new equilibrium solves $I_{ion}(v^*, m_\infty(v^*), n_\infty(v^*), h_\infty(v^*)) = 0$. For our parameter values, the right hand side in (9) is $0.036v^*$. The resting states of the MHH and DHH models are close. Applying the active node approximation to the DHH model, equation (20) characterizing propagation failure is replaced by:

$$I_{ion}(v_{j_0}, m_\infty(v_{j_0}), n^*, h^*) = D_d(V - 2v_{j_0} + v^*). \tag{26}$$

They differ in the factors $\frac{2D_d\gamma}{e^\gamma - e^{-\gamma}} = 0.97D_d$ and $e^\gamma + e^{-\gamma} = 2.2$. The parameter regions for propagation failure are similar for our parameter values.

However, if we wish to study the way variations of parameters in the myelin sheath affects nerve propagation, the DHH model is almost useless. The only parameter representing the myelin sheath in the simplified model is $D_d = \frac{1}{(R_i + R_e)LC_n\lambda_M}$, which involves the length of the myelin sheath. If this length changes noticeably, this means that the Ranvier nodes have increased their size, so as to not be identifiable with points, and the whole model should be changed. The DHH model cannot describe the impact of alterations in the myelin capacitance C_m or resistance R due to changes in the thickness of the myelin sheath. With even simpler FitzHugh–Nagumo approximations, all quantitative information is lost.

5 Propagation Failure Due to Vanishing Peaks

We have seen that inadequate values of resistances, conductances, capacitances, and so on, forbid nerve impulse propagation due to pinning of the leading front of the

impulse. Inadequate separation of time scales may also be a cause for propagation failure. By studying the width of the peak we can find thresholds for the separation of scales ε .

Throughout the peak (region (III) in Fig. 6(a)), the slow variables vary in their length scale $\tau = \varepsilon t$ (recall that $\varepsilon = \lambda_n$) and the fast variables relax instantaneously to their equilibrium values: $m_j(t) = m_\infty(v_j(t))$ with $v_j(t)$ satisfying

$$I_{\text{ion}}(v_j(t), m_\infty(v_j(t)), n_j(t), h_j(t)) = D_d[G^+(v_j(t), v^*) - G^-(V, v_j(t))]. \tag{27}$$

In the quasistatic approximation $G^+(v_j, v_{j+1}) - G^-(v_{j-1}, v_j)$ becomes $(v_{j+1}(t) - v_j(t)(e^\gamma + e^{-\gamma}) + v_{j-1}(t))\frac{2\gamma}{e^\gamma - e^{-\gamma}}$; see Sect. 2. Now, $v_j(t) \sim v_{j+1}(t) \sim v_{j-1}(t)$ in the peak and (27) reduces to

$$g_{\text{Na}}m_\infty(v_j(t))^3 h_j(t)(v_j(t) - 1) + g_L(v_j(t) - V_L) + g_K(n_j(t))^4 (v_j(t) - V_K) = 2D_d\gamma \frac{1 - \cosh(\gamma)}{\sinh(\gamma)} v_j(t). \tag{28}$$

Figure 2(b) shows that this type of equations has typically three branches of zeros v_j for known n_j, h_j . Since the peak is matched to the leading front, v_j must lie in the third branch of zeros: $v_j = v^{(3)}(n_j, h_j)$ and $m_j = m_\infty(v_j)$. The slow variables (n_j, h_j) are governed by the slow system:

$$\frac{dn_j}{d\tau} = \Lambda_n(v_j)[n_\infty(v_j) - n_j], \quad \frac{dh_j}{d\tau} = \lambda \Lambda_h(v_j)[h_\infty(v_j) - h_j], \tag{29}$$

for $\tau_0 < \tau < \tau_1$ and lie in an integral curve of

$$\frac{dh}{dn} = \frac{\lambda \Lambda_h(v^{(3)}(n, h))[h_\infty(v^{(3)}(n, h)) - h]}{\Lambda_n(v^{(3)}(n, h))[n_\infty(v^{(3)}(n, h)) - n]}, \quad h(n^*) = h^*. \tag{30}$$

In standard asymptotic constructions of pulses, the peak ends in a trailing front through which the slow variables remain near constant values (n_1^*, h_1^*) lying in the integral curve (30) (Carpio and Bonilla 2003b; Carpio 2005b; Keener 1980). These values are selected observing that the back front must move at the same speed as the leading front, which is determined by (n^*, h^*) . For some nonlinearities it may happen that no trailing fronts moving at the required speed exist. In that case, the peak ends at values (n_1^*, h_1^*) for which the branch $v^{(3)}$ is lost. Numerical simulations suggest that this might often be the case for our strongly asymmetric source, as in Carpio (2005a).

The time length of the peak of the impulse is found by integrating (29):

$$\mathcal{T}_1 = \frac{\tau_1 - \tau_0}{\varepsilon} = \int_{n^*}^{n_1^*} \frac{ds}{\varepsilon \Lambda_n(v^{(3)}(s, h(s)))[n_\infty(v^{(3)}(s, h(s))) - s]}, \tag{31}$$

where the integral is evaluated along the solution $h(n)$ of (30). The number of Ranvier nodes in the peak is computed using the traveling wave structure: $v_j(t) = v(j - ct)$. The temporal length \mathcal{T}_1 is the time delay between the instant at which the leading

front is placed at the j th node and the time at which the end of the peak is located at the same node. The number of nodes forming the peak is then the closest integer to:

$$L_1 \sim c(n^*, h^*)T_1. \tag{32}$$

The above construction is only consistent if $L_1 \geq 1$. This provides a restriction on the size of ϵ for the existence of pulses:

$$\epsilon \leq c(n^*, h^*) \int_{n^*}^{n_1^*} \frac{ds}{\Delta_n(v^{(3)}(s, h(s)))[n_\infty(v^{(3)}(s, h(s))) - s]}. \tag{33}$$

The quality of these approximations is tested in Fig. 8(c)–(e).

6 Conclusions

We have analyzed saltatory propagation of impulses in the MHH model for myelinated fibers. Nerve impulses consist of two parts: a discrete traveling pulse at the Ranvier nodes (which solves an integrodifferential system for the voltage at the nodes) and a subordinated continuous wave propagating through the internodal regions (induced by the dynamics of the nodes). The internodal region affects the generation and propagation of the discrete traveling pulse through a number of parameters describing properties of the myelin sheath, which enter the integrodifferential system governing the impulse at the Ranvier nodes.

Simple analytical characterizations of the parameter regions (resistances, conductances, rates, ...) for which propagation fails, together with predictions of the speed and width of the impulse, have been given by exploiting separation of time scales and truncations to small subsystems of active nodes. These predictions are in good agreement with numerical simulations of the full model. In contrast to previous work on propagation failure in discrete equations, the leading fronts of our impulses solve discrete bistable systems for which no comparison principles are available.

Unlike simpler models, the MHH system provides quantitative information, suitable for comparison with experimental data. It incorporates precise information on the myelin sheath, allowing to test the influence of damage in the myelin cover on nerve propagation. The models we have discussed consider single fibers. Nerves are usually formed by bundles of fibers. Our analysis of single myelinated fibers might serve as a basis for the study of impulse propagation along nerve bundles following the ideas in Binczak et al. (2001).

Acknowledgements This work has been supported by the Spanish Ministry of Research and the Autonomous Region of Madrid under Grants FIS2008-04921-C02-02 and CM-910143.

Appendix A

The myelinated Hodgkin–Huxley model was proposed in FitzHugh (1962). We recall its structure. Let us denote by $V(X, T)$ and $V_j(T)$ the deviation of the potential

with respect to its equilibrium value in the myelin sheaths and at the Ranvier nodes, respectively. We assume that the nodes are separated by a distance L , equal to the length of the myelin sheath. The length of the myelin sheaths is of order 1–2 mm (about $100d$, where d is the fiber diameter). The length of the Ranvier nodes is of order $1 \mu\text{m}$. Therefore, we may consider the Ranvier nodes simply as points located at positions X_j . Myelin covers the intervals $[X_j, X_{j+1}]$. The time evolution of the voltage $V(X, T)$ in the myelin sheaths (see FitzHugh 1962) is governed by

$$C_m \frac{\partial V}{\partial T} = \frac{1}{\bar{R}_i + \bar{R}_e} \frac{\partial^2 V}{\partial X^2} - \frac{V}{\bar{R}}, \quad X \in (X_j, X_{j+1}), \quad T > 0, \tag{34}$$

$$V(X_j, T) = V_j(T), \quad V(X_{j+1}, T) = V_{j+1}(T). \tag{35}$$

These equations are coupled with equations for the voltage at the nodes (FitzHugh 1962):

$$C_n \frac{dV_j}{dT} + \bar{I}_{\text{ion}}(V_j, M_j, N_j, H_j) = \frac{1}{\bar{R}_i + \bar{R}_e} \left[\frac{\partial V}{\partial X}(X_j^+, T) - \frac{\partial V}{\partial X}(X_j^-, T) \right]. \tag{36}$$

The ion current through the membrane is given by

$$\begin{aligned} \bar{I}_{\text{ion}}(V, M, N, H) = & \bar{g}_{\text{Na}} M^3 H (V - \bar{V}_{\text{Na,R}}) \\ & + \bar{g}_L (V - \bar{V}_{\text{L,R}}) + \bar{g}_K N^4 (V - \bar{V}_{\text{K,R}}). \end{aligned} \tag{37}$$

The dimensionless variables N_j , M_j and H_j control the chemistry of sodium and potassium: N_j is the potassium activation, M_j the sodium activation and H_j the sodium inactivation. Their dynamics obeys the equations:

$$\begin{aligned} \frac{dM_j}{dT} &= \bar{\lambda}_M \bar{\Lambda}_M(V_j) (M_\infty(V_j) - M_j), \\ \frac{dN_j}{dT} &= \bar{\lambda}_N \bar{\Lambda}_N(V_j) (N_\infty(V_j) - N_j), \\ \frac{dH_j}{dT} &= \bar{\lambda}_H \bar{\Lambda}_H(V_j) (H_\infty(V_j) - H_j). \end{aligned} \tag{38}$$

Parameters have the following meaning. \bar{g}_{Na} and \bar{g}_K are the maximum conductances for Na^+ and K^+ channels, respectively. \bar{g}_L is the leakage conductance. The corresponding potentials are \bar{V}_{Na} , \bar{V}_K and \bar{V}_L , respectively. We define, $\bar{V}_{\text{Na,R}} = \bar{V}_{\text{Na}} - \bar{V}_R$, $\bar{V}_{\text{K,R}} = \bar{V}_K - \bar{V}_R$ and $\bar{V}_{\text{L,R}} = \bar{V}_L - \bar{V}_R$, where \bar{V}_R is the resting potential. C_n is the capacitance of the membrane at the nodes and C_m the myelin capacitance. \bar{R}_i and \bar{R}_e represent intracellular and extracellular membrane resistances. \bar{R} is the myelin resistance. Myelin may increase the electrical resistance across the membrane by a factor of 5 000 and decrease its capacitance by a factor of 50.

In the literature on the Hodgkin–Huxley models, convergence rates are usually represented as single functions $\bar{\Lambda}_\ell(V)$. We have chosen to write $\bar{\lambda}_\ell \bar{\Lambda}_\ell(V)$ so that nondimensionalizing the model becomes easier. Our parameter $\bar{\lambda}_\ell$ contains the units

Table 2 Parameter values for a myelinated frog nerve

C_m	\bar{V}_{Na}	$\bar{R}_i + \bar{R}_e$	\bar{g}_{Na}	$\bar{\lambda}_M$
1.6 pf/mm	47 mV	15 MΩ/mm	0.57 μmho	127 (ms) ⁻¹
C_n	\bar{V}_K	\bar{R}	\bar{g}_K	$\bar{\lambda}_H$
1.5 pf	-75 mV	290 MΩmm	0.104 μmho	1.76 (ms) ⁻¹
\bar{V}_R	\bar{V}_L	L	\bar{g}_L	$\bar{\lambda}_N$
-70 mV	-75 mV	2 mm	0.025 μmho	2 (ms) ⁻¹

Table 3 Nondimensionalization rules

g_{Na}	g_K	g_L	D_d	D_c	R	V_K	V_L	λ_n	λ_h
$\frac{\bar{g}_{Na}}{C_n \bar{\lambda}_M}$	$\frac{\bar{g}_K}{C_n \bar{\lambda}_M}$	$\frac{\bar{g}_L}{C_n \bar{\lambda}_M}$	$\frac{\bar{D}}{C_n \bar{\lambda}_M}$	$\frac{\bar{D}}{C_m \bar{\lambda}_M L}$	$\bar{R} C_m \bar{\lambda}_M$	$\frac{\bar{V}_{K,R}}{\bar{V}_{Na,R}}$	$\frac{\bar{V}_{L,R}}{\bar{V}_{Na,R}}$	$\frac{\bar{\lambda}_N}{\bar{\lambda}_M}$	$\frac{\bar{\lambda}_H}{\bar{\lambda}_M}$

and also the order of magnitude of the term. For the motor nerves of frogs (Cole 1968), experimental curves can be adjusted using the following profiles:

$$\begin{aligned}
 \bar{\Lambda}_M(V) &= 0.03 \left[\frac{2.5 - 0.1V}{\exp(2.5 - 0.1V) - 1} + 4 \exp\left(\frac{-V}{18}\right) \right], \\
 M_\infty(V) &= \left[1 + 4 \exp\left(\frac{-V}{18}\right) \frac{\exp(2.5 - 0.1V) - 1}{(2.5 - 0.1V)} \right]^{-1}, \\
 \bar{\Lambda}_H(V) &= \left[0.07 \exp\left(\frac{-V}{20}\right) + \frac{1}{\exp(3 - 0.1V) + 1} \right], \\
 H_\infty(V) &= \left[1 + \frac{\exp\left(\frac{V}{20}\right)}{0.07(\exp(3 - 0.1V) + 1)} \right]^{-1}, \\
 \bar{\Lambda}_N(V) &= 0.79 \left[\frac{0.1 - 0.01V}{\exp(1 - 0.1V) - 1} + 0.125 \exp\left(\frac{-V}{80}\right) \right], \\
 N_\infty(V) &= \left[1 + 0.125 \exp\left(\frac{-V}{80}\right) \frac{\exp(1 - 0.1V) - 1}{(0.1 - 0.01V)} \right]^{-1},
 \end{aligned}
 \tag{39}$$

where V is measured in mV. Typical values for the remaining parameters are collected in Table 2 (Cole 1968; Scott 1975).

To nondimensionalize the model we introduce the new variables:

$$\begin{aligned}
 v &= \frac{V}{\bar{V}_{Na,R}}, & t &= T \bar{\lambda}_M, & x &= \frac{X}{L}, \\
 m_j &= M_j, & n_j &= N_j, & h_j &= H_j.
 \end{aligned}$$

Setting $\bar{D} = \frac{1}{(\bar{R}_e + \bar{R}_i)L}$, we obtain the dimensionless equations (1)–(4) of Sect. 1, with dimensionless parameters computed according to Table 3.

The new profiles $\Lambda_n(v)$, $\Lambda_m(v)$, $\Lambda_h(v)$ and $n_\infty(v)$, $m_\infty(v)$, $h_\infty(v)$ are obtained from the original ones replacing V by $v\sqrt{V_{Na,R}}$ in (39). All these functions take values in $(0, 1)$ for the ranges of interest of the variable v . Thus, the parameters λ_n, λ_h allow one to visualize the relevant time scales.

Appendix B

In this section we give an explicit formula for the operator $G^+(v_j, v_{j+1}) - G^-(v_{j-1}, v_j)$ entering (5). To do so, we need expressions for the solution $v = Q[v_j, v_{j+1}]$ of the parabolic problem (1)–(2). The first step is to replace this problem by an analogous one with zero boundary conditions. We set $v(x, t) = u(x, t) + q^+(x, t)$ in (x_j, x_{j+1}) . Then u solves

$$\frac{\partial u}{\partial t} - D_c \frac{\partial^2 u}{\partial x^2} + \frac{u}{R} = a^+, \quad x \in (x_j, x_{j+1}) = (j, j + 1), \quad t > 0, \tag{40}$$

$$u(x_j, t) = 0, \quad u(x_{j+1}, t) = 0, \tag{41}$$

$$u(x, 0) = b^+(x, 0), \tag{42}$$

with

$$a^+(x, t) = \frac{q^+(x, t)}{R} - \frac{\partial q^+}{\partial t}(x, t), \quad b^+(x, 0) = v(x, 0) - q^+(x, 0),$$

$$q^+(x, t) = v_j(t) \frac{x - x_{j+1}}{x_j - x_{j+1}} + v_{j+1}(t) \frac{x - x_j}{x_{j+1} - x_j}.$$

Let $\mu_\ell = D_c(\ell\pi)^2 + \frac{1}{R}$ and $\phi_\ell(x) = \sin(\sqrt{\mu_\ell}x)(\int_0^1 \sin(\sqrt{\mu_\ell}x)^2 dx)^{-1}$ be the eigenvalues and orthonormalized eigenfunctions of the operator $-D_c \frac{\partial^2 u}{\partial x^2} + \frac{u}{R}$ in $(0, 1)$ with zero boundary conditions. We expand a^+ and b^+ as a Fourier series of the eigenfunctions:

$$a^+(x, t) = \sum_{\ell=0}^{\infty} a_\ell^+(t) \phi_\ell(x - x_j), \quad a_\ell^+(t) = \int_0^1 a^+(z + x_j, t) \phi_\ell(z) dz,$$

$$b^+(x, 0) = \sum_{\ell=0}^{\infty} b_\ell^+(0) \phi_\ell(x - x_j), \quad b_\ell^+(0) = \int_0^1 b^+(z + x_j, 0) \phi_\ell(z) dz.$$

The solution of (1)–(2) is then given by

$$v^+(x, t) = q^+(x, t) + \sum_{\ell=0}^{\infty} e^{-\mu_\ell t} b_\ell^+(0) \phi_\ell(x - x_j) + \sum_{\ell=0}^{\infty} e^{-\mu_\ell t} \phi_\ell(x - x_j) \int_0^t e^{\mu_\ell s} a_\ell^+(s) ds, \tag{43}$$

where

$$a_\ell^+(t) = \left(\frac{v_j(t)}{R} - \frac{dv_j(t)}{dt} \right) A_\ell + \left(\frac{v_{j+1}(t)}{R} - \frac{dv_{j+1}(t)}{dt} \right) B_\ell, \tag{44}$$

with $A_\ell = \int_0^1 (1 - z)\phi_\ell(z) dz$ and $B_\ell = \int_0^1 z\phi_\ell(z) dz$. A similar expression holds for the solution $v^-(x, t)$ of (1)–(2) in (x_{j-1}, x_j) , replacing q^+ by q^- , a^+ by a^- , b^+ by b^- , a_ℓ^+ by a_ℓ^- , b_ℓ^+ by b_ℓ^- , v_{j+1} by v_j and v_j by v_{j-1} . Integrating by parts,

$$\begin{aligned} \int_0^t e^{\mu_\ell s} a_\ell^+(s) ds &= \left(\frac{1}{R} + \mu_\ell \right) A_\ell \int_0^t e^{\mu_\ell s} v_j(s) ds - A_\ell e^{\mu_\ell t} v_j(t) + A_\ell v_j(0) \\ &\quad + \left(\frac{1}{R} + \mu_\ell \right) B_\ell \int_0^t e^{\mu_\ell s} v_{j+1}(s) ds - B_\ell e^{\mu_\ell t} v_{j+1}(t) \\ &\quad + B_\ell v_{j+1}(0), \end{aligned}$$

and an analogous expression holds for a_ℓ^- .

The term $\frac{\partial v^+}{\partial x}(x_j^+, t) - \frac{\partial v^-}{\partial x}(x_j^-, t) = G^+(v_j, v_{j+1}) - G^-(v_{j-1}, v_j)$ takes the final form

$$\begin{aligned} &\sum_\ell e^{-\mu_\ell t} \frac{\partial \phi_\ell}{\partial x}(0) \left[\int_0^1 v(z + x_j, 0)\phi_\ell(z) dz - B_\ell v_{j+1}(0) - A_\ell v_j(0) \right] \\ &\quad - \sum_\ell e^{-\mu_\ell t} \frac{\partial \phi_\ell}{\partial x}(1) \left[\int_0^1 v(z + x_{j-1}, 0)\phi_\ell(z) dz - B_\ell v_j(0) - A_\ell v_{j-1}(0) \right] \\ &\quad + \sum_\ell e^{-\mu_\ell t} \frac{\partial \phi_\ell}{\partial x}(0) \left[\left(\frac{1}{R} + \mu_\ell \right) \int_0^t e^{\mu_\ell s} (B_\ell v_{j+1}(s) + A_\ell v_j(s)) ds \right. \\ &\quad \left. - e^{\mu_\ell t} (B_\ell v_{j+1}(t) + A_\ell v_j(t)) + (B_\ell v_{j+1}(0) + A_\ell v_j(0)) \right] \\ &\quad - \sum_\ell e^{-\mu_\ell t} \frac{\partial \phi_\ell}{\partial x}(1) \left[\left(\frac{1}{R} + \mu_\ell \right) \int_0^t e^{\mu_\ell s} (B_\ell v_j(s) + A_\ell v_{j-1}(s)) ds \right. \\ &\quad \left. - e^{\mu_\ell t} (B_\ell v_j(t) + A_\ell v_{j-1}(t)) + (B_\ell v_j(0) + A_\ell v_{j-1}(0)) \right] \\ &\quad + v_{j+1} - 2v_j + v_{j-1}. \tag{45} \end{aligned}$$

Appendix C

A simple method to numerically solve the dimensionless MHH model approximates by finite differences the derivatives appearing in (1) and (3):

$$\frac{\partial^2 v}{\partial x^2}(x, t) = \frac{v(x+r, t) - 2v(x, t) + v(x-r, t)}{r^2}, \quad x \in (j, j+1) = (x_j, x_{j+1}),$$

$$\frac{\partial v}{\partial x}(x_j^+, t) = \frac{v(x_j+r) - v(x_j, t)}{r}, \quad \frac{\partial v}{\partial x}(x_j^-, t) = \frac{v(x_j) - v(x_j-r, t)}{r}.$$

In each internodal space $[j, j+1]$ we introduce $N - 1$ numerical nodes. We set $r = \frac{1}{N}$ and denote by $y_{j,\ell} = j + \ell r$, $\ell = 0, \dots, N$, $j = 0, \dots, M$ the nodes. The index ℓ indicates the position of the numerical node in the internodal space $[j, j+1]$ determined by the index j . There are $M + 1$ Ranvier nodes in the fiber and $N + 1$ numerical nodes in each internodal space. We numerate all the nodes consecutively. Keeping j fixed we set $z_k = y_{j,\ell}$, $k = j + \ell r$, for $\ell = 0, \dots, N$ and then increase j from 0 to M . The Ranvier nodes are located in the positions z_{jN} , $j = 0, \dots, M$. At each Ranvier node, (3)–(4) hold. Discretizing the spatial derivatives we find

$$\begin{cases} \frac{dv_{jN}}{dt} + I(v_{jN}, m_{jN}, n_{jN}, h_{jN}) = D_d \frac{v_{jN+1} - 2v_{jN} + v_{jN-1}}{r}, \\ \frac{dm_{jN}}{dt} = \Lambda_m(v_{jN})[m_\infty(v_{jN}) - m_{jN}], \\ \frac{dn_{jN}}{dt} = \lambda_n \Lambda_n(v_{jN})[n_\infty(v_{jN}) - n_{jN}], \\ \frac{dh_{jN}}{dt} = \lambda_h \Lambda_h(v_{jN})[h_\infty(v_{jN}) - h_{jN}], \end{cases} \quad (46)$$

for $j = 1, \dots, M - 1$. At the intermediate numerical nodes, (1) yields

$$\frac{dv_\ell}{dt} - D_c \frac{v_{\ell+1} - 2v_\ell + v_{\ell-1}}{r^2} = -\frac{v_\ell}{R}, \quad \ell = jN + 1, \dots, (j+1)N - 1, \quad (47)$$

for $j = 0, \dots, M - 1$. Now, v_k, m_k, n_k, h_k stand for the values of the variables at the numerical nodes z_k . The resulting system of ordinary differential equations is then solved employing the MATLAB adaptive Runge–Kutta solver ode23 with relative error tolerance at least 10^{-3} . We typically set $M = 150$ – 200 and $N = 10$ – 100 .

References

Anderson, A.R.A., Sleeman, B.D.: Wave front propagation and its failure in coupled systems of discrete bistable cells modelled by FitzHugh–Nagumo dynamics. *Int. J. Bifurc. Chaos* **5**, 63–74 (1995)

Beeler, G.W., Reuter, H.: Reconstruction of the action potential of ventricular myocardial fibres. *J. Physiol.* **268**, 177–210 (1977)

Bell, J., Costner, C.: Threshold behavior and propagation for nonlinear differential-difference systems motivated by modelling myelinated axons. *Q. Appl. Math.* **42**, 1–13 (1984)

Binczak, S., Eilbeck, J.C., Scott, A.C.: Ephaptic coupling of myelinated nerve fibers. *Physica D* **148**, 159–174 (2001)

Carpio, A.: Asymptotic construction of pulses in the Hodgkin–Huxley model for myelinated nerves. *Phys. Rev. E* **72**, 011905 (2005a)

Carpio, A.: Wave trains, self-oscillations and synchronization in discrete media. *Physica D* **207**, 117–136 (2005b)

Carpio, A., Bonilla, L.L.: Wave front depinning transition in discrete one dimensional reaction-diffusion systems. *Phys. Rev. Lett.* **86**, 6034–6037 (2001)

Carpio, A., Bonilla, L.L.: Depinning transitions in discrete reaction-diffusion equations. *SIAM J. Appl. Math.* **63**, 1056–1082 (2003a)

- Carpio, A., Bonilla, L.L.: Pulse propagation in discrete systems of excitable cells. *SIAM J. Appl. Math.* **63**(2), 619–635 (2003b)
- Carpio, A., Chapman, S.J., Hastings, S., McLeod, J.B.: Wave solutions for a discrete reaction-diffusion equation. *Eur. J. Appl. Math.* **11**, 399–412 (2000)
- Casten, R.G., Cohen, H., Lagerstrom, P.A.: Perturbation analysis of an approximation to the Hodgkin–Huxley theory. *Q. Appl. Math.* **4**, 365–402 (1975)
- Cole, K.S.: *Membranes, Ions and Impulses*. University of California Press, Berkeley (1968)
- Coombes, S., Hinch, R., Timofeeva, Y.: Receptors, sparks and waves in a fire-diffuse-fire framework for calcium release. *Prog. Biophys. Mol. Biol.* **85**, 197–216 (2003)
- Fáth, G.: Propagation failure of traveling waves in a discrete bistable medium. *Physica D* **116**, 176–180 (1998)
- FitzHugh, R.: Impulses and physiological states in theoretical models of nerve membrane. *Biophys. J.* **1**, 445–466 (1961)
- FitzHugh, R.: Computation of impulse initiation and saltatory conduction in a myelinated nerve fiber. *Biophys. J.* **2**, 11–21 (1962)
- Goldman, L., Albus, J.S.: Computation of impulse conduction in myelinated fibres: Theoretical basis of the velocity-diameter relation. *Biophys. J.* **8**, 596–607 (1968)
- Hodgkin, A.L., Huxley, A.F.: A quantitative description of membrane current and its application to conduction and excitation in nerve. *J. Physiol.* **117**, 500–544 (1952)
- Keener, J.P.: Waves in excitable media. *SIAM J. Appl. Math.* **39**, 528–548 (1980)
- Keener, J.P.: Propagation failure in coupled systems of discrete excitable cells. *SIAM J. Appl. Math.* **47**, 317–334 (2000)
- Keener, J.P., Sneyd, J.: *Mathematical Physiology*. Springer, Berlin (1998)
- Mallet-Paret, J.: The global structure of traveling waves in spatially discrete dynamical systems. *J. Dyn. Differ. Equ.* **11**, 1–47 (1999)
- Markin, V.S., Chimadzhev, Yu.A.: On the propagation of an excitation for one model of a nerve fiber. *Biophys. J.* **12**, 1032–1040 (1967)
- Morris, C., Lecar, H.: Voltage oscillations in the barnacle giant muscle fiber. *Biophys. J.* **35**, 193–213 (1981)
- Moore, J.W., Joyner, R.W., Brill, M.H., Waxman, S.D., Najjar-Joa, M.: Simulations of conduction in uniform myelinated fibers: Relative sensitivity to changes in nodal and internodal parameters. *Biophys. J.* **21**, 147–160 (1978)
- Muratov, C.B.: A quantitative approximation scheme for traveling wave solutions in the Hodgkin–Huxley model. *Biophys. J.* **79**, 2893–2901 (2000)
- Nagumo, J., Arimoto, S., Yoshizawa, S.: An active pulse transmission line simulating nerve axon. *Proc. Inst. Radio Eng.* **50**, 2061–2070 (1962)
- Pickard, W.F.: On the propagation of the nervous impulse down medullated and unmedullated fibers. *J. Theor. Biol.* **11**, 30–40 (1966)
- Pluchino, S., Quattrini, A., Brambilla, E., et al.: Injection of adult neurospheres induces recovery in a chronic model of multiple sclerosis. *Nature* **422**, 688–694 (2003)
- Ponce Dawson, S., Keizer, J., Pearson, J.E.: Fire-diffuse-fire model of dynamics of intracellular calcium waves. *Proc. Natl. Acad. Sci. USA* **96**, 6060–6063 (1999)
- Rinzel, J., Keller, J.B.: Traveling wave solutions of a nerve conduction equation. *Biophys. J.* **13**, 1313–1337 (1973)
- Rushton, W.A.H.: A theory of the effects of fibre size in medullated nerve. *J. Physiol.* **115**, 101–122 (1951)
- Scott, A.C.: The electrophysics of a nerve fiber. *Rev. Mod. Phys.* **47**, 487–533 (1975)
- Scott, A.C.: *Neuroscience*. Springer, Berlin (2002)
- Struijk, J.J.: The extracellular potential of a myelinated nerve fiber in an unbounded medium and in nerve cuff models. *Biophys. J.* **72**, 2457–2469 (1997)
- Timofeeva, Y.: Travelling waves in a model of quasi-active dendrites with active spines. *Physica D* **239**, 494–503 (2010)
- Tonneller, A.: The McKean's caricature of the FitzHugh-Nagumo model: Traveling pulses in discrete diffusive medium. *Phys. Rev. E* **67**, 036105 (2003)
- Zinner, B.: Existence of traveling wave front solutions for the discrete Nagumo equation. *J. Differ. Equ.* **96**, 1–27 (1992)